Electronic Supplementary Material (ESI) for Nanoscale.
This journal is © The Royal Society of Chemistry 2014

Supplementary Information

The rational nanostructuring of surfaces for extraordinary icephobicity

Patric Eberle, Manish K. Tiwari, Tanmoy Maitra and Dimos Poulikakos**
*Corresponding Authors**

1. Thermodynamic Relations and Poisson Statistics

The thermodynamically guided tailoring of surface morphologies aims at depressing the heterogeneous ice nucleation rate by unfavorable thermodynamic conditions stemming from the surface/droplet interaction. The theoretical framework for this surface morphology tailoring can be established by invoking the use of the classical heterogeneous nucleation theory (CNT), which predicts the rate of formation of a critically sized ice embryo to be[1-3]

$$J(T) = K(T) A \exp\left(\frac{-\Delta G(T)}{k_B T}\right) \quad , \tag{S1}$$

where *K, A, ΔG* and k_B respectively denote a kinetic prefactor accounting for the diffusive flux of water molecules across the ice surface, the droplet-substrate contact area, the free energy barrier to form the critical ice embryo and the Boltzmann constant. The free energy barrier in Equation S1 can be expressed as[1, 2]

$$\Delta G(T, \Theta_{IW}, R) = \frac{16\pi \gamma_{IW}{}^{3}}{3(\Delta G_{f,v}(T))^{2}} f(\Theta_{IW}, R) \quad , \tag{S2}$$

where $\gamma_{IW}(T)$, $\Delta G_{f,v}(T)$, *f*, $\Theta_{IW}(T,R)$ and *R* denote the ice-water interfacial energy, the volumetric free energy difference per unit volume between water and ice, a factor relating the energy barrier for homogeneous nucleation to heterogeneous nucleation, the contact angle of the ice embryo (ice-water), and the roughness curvature radius, respectively. From the Gibbs-

Helmholtz Equation it follows that $\Delta G_{f,v} = \Delta H_{f,v}\,(T_m - T)/T_m$. Naturally, $f = 1$ corresponds to homogeneous ice nucleation. From Equation S2, it can be shown that at −25 °C, a typical temperature of our interest, the critical ice embryo radius [1, 2] is $r_c = 2\gamma_{IW}/\Delta G_{f,v} \approx 1.7$ nm (with $\Delta H_{f,v} = 278$ MJ/m^3 and $\gamma_{IW} = 2.17$ mJ/m^2). To calculate the nucleation parameters needed in this work, use was made of general temperature dependent empirical relations for the values of interfacial energy and enthalpy of fusion (Equation 5-12 and 3-16 in [1]).

The kinetic prefactor $K(T)$ in Equation S1 can be related to the diffusion activation energy of a water molecule needed to cross the water-ice interface[1, 3]

$$K(T) = \frac{k_B T}{h} \exp\left(\frac{-\Delta F_{diff}(T)}{k_B T}\right) n \quad , \qquad \text{(S3)}$$

where k_B, h, ΔF_{diff} and n are the Boltzmann constant, the Planck constant, the diffusion activation energy of a water molecule to cross the water-ice embryo interface and the number density of water molecules at the ice nucleus/water interface ($n \approx 10^{19}$ m^{-2}), respectively. The growth rate of ice in a supercooled droplet can be estimated by using the kinetic prefactor $K(T)$ from Equation S3 multiplied by the contact area of the droplet. For a droplet with representative volume of 4 µL and CA of 100°, the ice growth rates are tabulated in Table S1 at three different temperatures.

Table S1. Estimated growth rate of ice in a 4 µL droplet for a representative CA = 100°

T [°C]	-30	-25	-20
Growth rate of ice [molecules/second]	~1.9 x 10^{20}	~4.3 x 10^{20}	~8.9 x 10^{20}

The diffusion activation energy is defined as[4]

$$\Delta F_{diff}(T) = \frac{\partial \ln D(T)}{\partial T} k_B T^2 \quad , \tag{S4}$$

where D is the diffusivity of water which can be expressed by the empirical Vogel-Fulcher-Tammann Equation as[5]

$$D(T) = D_0 \exp\left[\frac{-E}{T - T_R}\right] \quad , \tag{S5}$$

where D_0, E and T_R are fit parameters. Thus, Equation S4 can be rewritten as

$$\Delta F_{diff}(T) = \frac{k_B T^2 E}{(T - T_R)^2} \quad . \tag{S6}$$

For liquid water, the values of E = 892 K and T_R = 118 K have been determined experimentally in the temperature range from 150 K to 273 K.[5]

For a small change in temperature ΔT around a reference temperature T_0, the free energy term in Equation S1 can be linearized to obtain

$$\frac{\Delta G(T_0 + \Delta T)}{k_B T} = \frac{\Delta G(T_0)}{k_B T} + \frac{\partial}{\partial T}\left(\frac{\Delta G(T)}{k_B T}\right)\Bigg|_{T_0} \Delta T \, . \tag{S7}$$

Similarly, the diffusion activation energy of Equation S3 can be linearized as

$$\frac{\Delta F_{diff}(T_0 + \Delta T)}{k_B T} = \frac{\Delta F_{diff}(T_0)}{k_B T_N} + \frac{\partial}{\partial T}\left(\frac{\Delta F_{diff}(T)}{k_B T}\right)(T_0)\,\Delta T \quad . \tag{S8}$$

Combination of Equation S1, S3, S7 and S8 yields an approximation of the ice nucleation rate as

$$J(T_0 + \Delta T) \approx \frac{k_B T_0}{h} nA \exp\left(-\frac{\Delta F_{diff}(T_0 + \Delta T) + \Delta G(T_0 + \Delta T)}{k_B T_0}\right) = a \exp(-\lambda \Delta T) \quad , \tag{S9}$$

where a and λ are substrate-specific constants at the temperature T_0. Given the strong increase in ice nucleation rate with a decrease in temperature based on Equation S1 we can understand that at some point this rate becomes appreciable, e.g. attains the value of one embryo per second ($J(T_1) = 1\ \mathrm{s}^{-1}$).[2] In our case the ice nucleation rate becomes appreciable when the temperature reaches the value of the nucleation temperature T_N. The term nucleation temperature T_N refers to the median temperature at which ice nucleates in a sessile water droplet placed on a surface when the entire droplet/surface/surrounding gas system is at a uniform temperature and is cooled in a slow, quasi-steady manner (see main paper). For simplicity, T_0 of Equation S9 is selected close to the T_N. Although the starting temperature of the experiments T_S was higher than T_N, Equation S9 can still be used to calculate the T_N of the distribution. This is because the exponential dependence of the ice nucleation rate on temperature of Equation S9 ensures that the rate vanishes for temperatures only a few Kelvin higher than T_N.

For the following derivations, it is convenient to reference Equation S9 to the experimental starting temperature T_S, which is selected to be sufficiently high, so that the nucleation rate is very small $J(T_S) << 1$. This derivation is needed to predict the nucleation temperature of a substrate when the sessile droplet is cooled at a constant rate (as was the case for the experimental results shown in the box plots of Fig. S1a and 3b). Therefore, for a temperature deviation of ΔT_S around T_S we obtain

$$J(T_0 + \Delta T) = a\exp(-\lambda(T_S - T_0 + \Delta T_S)) = a_S \exp(-\lambda \Delta T_S) \quad , \qquad \text{(S10)}$$

where $\Delta T = T_S - T_0 + \Delta T_S$. In Equation S10, $a_S << 1$. The temperature variation during an experiment can be described by a simple linear time relation

$$\Delta T_S = \alpha t \quad , \qquad \text{(S11)}$$

where α is the rate of temperature change per unit time.

During nucleation temperature determination experiments, the ice nucleation rate continuously increased with the steady reduction in temperature, see Supplementary Information, section 9. The stochastic freezing with changing nucleation rate can be described by a nonhomogeneous Poisson process.[6] Therefore, employing Equation S10 and S11, we can express the probability density function for the life-time of the liquid droplet as

$$p(t) = J(t)\exp\left(-\int_0^t J(u)du\right) = a_S \exp(-\lambda\alpha t)\exp\left(\frac{-a_S}{\lambda\alpha}\left[1-\exp(-\lambda\alpha t)\right]\right), \tag{S12}$$

where use has been made of Equation S11 to express J as a function of time. Integration of Equation S12 yields the probability function of the frozen droplet

$$P(t) = \int_0^t p(u)du = 1-\exp\left(\frac{-a_S}{\lambda\alpha}\left[1-\exp(-\lambda\alpha t)\right]\right). \tag{S13}$$

The median freezing temperature, which is defined in this work as the median nucleation temperature (T_N), and median freezing time can be derived from Equation S13 by setting $P(t_{med}) = 0.5$, yielding

$$T_N = \frac{-1}{\lambda}\ln\left(1-\ln(2)\frac{\lambda\alpha}{a_S}\right)+T_S = \frac{-1}{\lambda}\ln(-\alpha\lambda\ln(2))+T_I \quad \text{and} \tag{S14}$$

$$t_{med} = \frac{-1}{\lambda\alpha}\ln\left(1-\ln(2)\frac{\lambda\alpha}{a_S}\right) = \frac{-1}{\lambda\alpha}\left[\ln\left\{-\lambda\alpha\ln(2)\right\}+\lambda(T_S-T_I)\right], \tag{S15}$$

where T_I is the temperature at which the nucleation rate becomes one embryo per second (i.e., $J(T_I) = 1\ \mathrm{s}^{-1}$). In deriving the expressions for T_N and t_{med} use was made of the fact that $\left(\lambda\alpha/a_S\right) >> 1$.

Employment of Equations S9 and S14, yields the nucleation rate at the median nucleation temperature as

$$J(T_N) = J(T_0 + \Delta T) = -\alpha\lambda \ln(2) . \qquad \text{(S16)}$$

If the contact area of a droplet is reduced by microstructuring, the ice nucleation rate of Equation S1 decreases by a factor equal to the contact area ratio, i.e. by $\frac{A_H \Phi_{S,\mu}}{A_N}$, where A_H and A_N are the apparent contact areas of hierarchical and only nanostructured surface and $\Phi_{S,\mu}$ denotes the ratio of solid area to the apparent contact area of the micro-structure under the droplet, respectively. For our pillar geometry $\Phi_{S,\mu} = \frac{a^2\pi}{p^2}$, where a is the radius and p the pitch of the pillars, respectively. By employing this factor and Equation S9 one obtains for the change in nucleation temperature for hierarchical substrates

$$T_{N,H} - T_{N,N} = \frac{-1}{\gamma} ln\left(\frac{A_N}{A_H \Phi_{S,\mu}}\right) \quad , \qquad \text{(S17)}$$

where $T_{N,H} - T_{N,N}$ is the difference in nucleation temperature between hierarchical and only nanostructured surfaces.

2. Ice Nucleation Delay Statistics and Measurements

In the case of ice nucleation delay experiments, the ice nucleation rate was constant as the experimental temperature was maintained at a constant value, see Supplementary Information, section 9. Therefore, a homogeneous Poisson process is employed to model the freezing yielding the probability density

function of the lifetime of a liquid droplet (before freezing) as

$$p_c(t) = J(T)\exp\left(-J(T)t\right) \qquad \text{(S18)}$$

and the probability function for droplet freezing as

$$P_c(t) = \int_0^t p_c(u)du = 1 - \exp\left(-J(T)t\right)$$

$$. \qquad \text{(S19)}$$

The subscript c is used to emphasize that these variables are for constant temperature case. Denoting ice nucleation delay by τ, we can employ Equation S18 to obtain the expected delay at a given temperature (i.e. expected value of the freezing delay time) as

$$\langle \tau \rangle = \int_0^\infty u p_c(u) du = \frac{1}{J(T)} . \qquad \text{(S20)}$$

This expected average delay time can also be related to the experimentally measured average ice nucleation delay (τ_{av}) as

$$\langle \tau \rangle \approx \tau_{av} = \frac{1}{n} \sum_{x=1}^{n} \tau_x , \qquad \text{(S21)}$$

where n is the number of droplets tested and τ_x the delay of a particular droplet.

The approximation in Equation S21 is equal for $n \to \infty$. In practice, the number of measurements is finite. However, for $J(T)$ and τ_{av} values so measured, we can calculate the statistical uncertainty by Poisson statistics, which for a given confidence level yields a lower and upper bound for the real value.[7]

Fig. S1a-c show box plots of ice nucleation delays (τ_x) measured at four different temperatures on the superhydrophobic surface A1-N1, the hydrophobic nanostructured substrate N1 and the hydrophilic surface N9, respectively. The averages of the measured delays τ_{av}, calculated using Equation S21, are plotted as circles. The probability density function for liquid droplets in nucleation delay experiments, i.e. the constant temperature experiments described by Equation S18 is confirmed in the Fig. S1e.

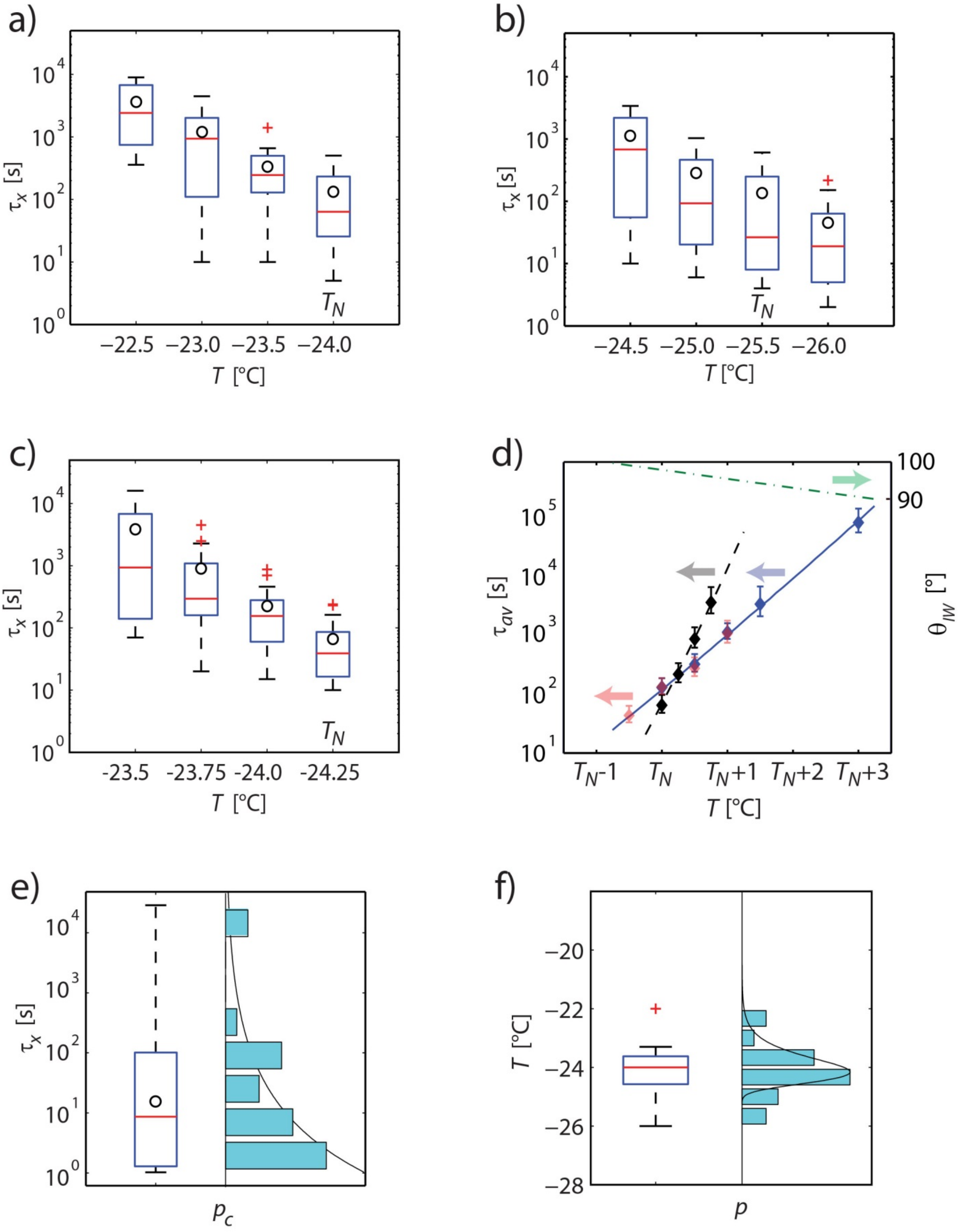

Fig. S1 Nucleation delays and temperatures of a sessile droplet (4µL) on substrate A1-N1. Box plots of nucleation delays at constant temperature for four different experimental temperature conditions for a) hierarchical substrate A1-N1, b) hydrophobic nanostructured surface N1 and c) hydrophilic nanostructured substrate N9. In b), the measurements for a second batch of fabricated N1 surfaces are shown where T_N is about 1.5 °C lower compared to the first batch (value shown in Fig. 2a). The slight natural variability in the arrangement of the FDTS monolayer coating between fabrication batches has a small effect on Θ_{IW} and T_N. d) Illustrating the increase in average ice nucleation delay (τ_{av}) of different substrates with increasing temperature. The error bars show the statistical uncertainty of τ_{av} calculated from Poisson statistics for a confidence level of 95%.[7] The blue diamonds correspond to the hierarchical substrate A1-N1 from a), the red diamonds to hydrophobic nanostructured surface N1 from b) and the black ones to the hydrophilic substrate N9 from c). The symbols represent the measured values. For a hydrophilic sample, a constant Θ_{IW} is adequate to match nucleation theory and measurements. On both hydrophobic samples, the predictions of nucleation theory (blue solid line) are in excellent agreement with the measurements by accounting for a linear decrease in Θ_{IW} with increasing temperature (green dash dotted line). Substrate N1 and N9 differ only in the FDTS monolayer which shows the FDTS monolayer being responsible for the temperature dependence of Θ_{IW}. Notwithstanding the greater slope for hydrophilic N9, the low ice adhesion and dynamic droplet impact resistance make the hierarchical substrates preferable for icephobicity. e) Box plot of nucleation delay measurements at $T = -23$ °C and the corresponding probability density p_c of the delay data shown as bars. The solid line represents the theoretically expected probability density function, see Equation S18. f) Box plot of nucleation temperatures measurements. The probability density function, p, of the measured nucleation temperatures is denoted by bars, and the solid line represents the expected probability density function according Equation S12.

3. Predicting Average Nucleation Delay around the Median Nucleation Temperature

Fig. S1d shows the measured τ_{av} values from Fig. S1a-c, plotted using blue, red and black diamonds for the surfaces A1-N1, N1 and N9, respectively. The error bars represent the statistical uncertainty of the measured τ_{av} from Poisson statistics for a confidence level of 95%.[7] Note that at the highest temperature $T = T_N + 3$ °C, τ_{av} was calculated from the ice nucleation rate $J\left(T_N + 3\right)$ by using Equation S20. The nucleation rate $J\left(T_N + 3\right)$ was measured using the relation[3] $J\left(T_N + 3\right) = \frac{n_1}{n\Delta t}$, where $n_1 = 12$ droplets nucleated in time Δt from a total of $n = 54$ droplets. This alternative but plausible approach had to be used at $T_N + 3$ °C due to the limited capacity of the liquid nitrogen tank for this extremely large nucleation delay time. It took $\Delta t = 5$ hours and 40 minutes for 12 droplets to freeze. For all the other temperatures investigated, the reported average delay times (τ_{av}) were obtained by directly observing and recording the freezing of the entire batch of tested droplets.

Substitution from Equation S1 and S2 in Equation S20, yields the predicted average delay at a given temperature $\left\langle \tau\left(T\right)\right\rangle$. This result can be compared with the measured $\tau_{av}\left(T\right)$ using the unknown Θ_{IW} as a fit parameter. Accounting for the temperature dependence of Θ_{IW}, leads to good agreement between predicted and measured results for the superhydrophobic A1-N1 surface and hydrophobic substrate N1. In Fig. S1c, an assumed linear decrease in Θ_{IW} of ~ −2.5°/K, yielded practically perfect coincidence between the calculated average delay $\left\langle \tau\left(T\right)\right\rangle$ (blue solid line) and the measurements for surface A1-N1 and N1 shown by the blue and red diamonds, respectively. The introduced decrease in contact angle Θ_{IW} with increase in temperature is entirely rational and should be understood in the context of the flexibility of the FDTS molecule, which was used to form the low surface energy monolayer.

The FDTS monolayer consists of weakly interacting, flexible fluorinated alkylsilane chains [8], which can readily adapt to the nucleating ice structures. This is a well-recognized behavior of long chain molecules. A similar observation was made for the nucleation rate of water droplets coated by a nonadecanol monolayer.[3] Our premise of the FDTS monolayer being responsible for the Θ_{IW} variation, is confirmed by the fact that the measured average delays (τ_{av}) of hydrophilic surface N9, i.e. a non-functionalized surface, are in very good agreement to the predictions of a constant Θ_{IW} of 100°. We note here that substrate N1 and N9 differ only in the presence of the FDTS monolayer on the former. Another important observation is that the slope of the τ_{av} temperature relation does not depend on the effective contact area between the droplet and the substrate. The superhydrophobic substrate A1-N1 and the hydrophobic nanostructured surface show practically the same slope which is in prefect agreement with the nucleation theory (see Equation S1, S2 and S20).

The greater slope of the τ_{av} with temperature on the hydrophilic nanostructured surface compared to the hierarchical superhydrophobic surface, may encourage the option to use hydrophilic surfaces for anti-icing. However, hydrophilic surfaces come with significantly larger ice adhesion, which was recently shown to correlate with receding contact angle.[9] In fact, our estimates show[9] nearly two orders of magnitude larger ice adhesion for the hydrophilic surfaces relative to the hierarchical A1-N1 surface. Furthermore, dynamic droplet impact resistance[10] is another desired property of icephobic surfaces. In Supplementary Information, section 8, we also show that water droplet impacting on the hydrophilic substrate N9 adhere, but they bounce completely off on a typical hierarchically structured hydrophobic surface C1-N2. Therefore, in this work we decided to render superhydrophobic surfaces with thermodynamically guided tailoring of the hierarchical morphologies to circumvent such disadvantages of hydrophilicity.

The temperature dependent change in Θ_{IW} and its influence on the nucleation delay is one pathway of interpreting the measured average ice nucleation delays (τ_{av}). As alternate and simpler approach, we can employ the approximation Equation S9 to predict the change in τ_{av} around a reference temperature, i.e. nucleation temperature. Equation S9 is fitted to the experimentally determined $\tau_{av}(T)$ to obtain the scaling factor $exp(-\lambda.1K) \approx 10^{-1}$. On the other hand, through cooling experiments, the median nucleation temperature was determined to be $T_N = -24$ °C, see Fig. 3a and S1e. At this temperature, the average measured ice nucleation delay is $\tau_{av} = 133$ s according to Fig. S1a and S1c. If the average ice nucleation delay data are extrapolated by using Equation S9 to only 3 Kelvin higher than the nucleation temperature, the average ice nucleation delay should reach ~27 hours. As depicted by Fig. S1c, this coincides very well with the measured $\tau_{av}\left(T_N+3\right) \approx 25$ hours.

To further establish the consistency between the results of the nucleation temperature and ice nucleation delay experiments, we compare the Poisson statistics-based prediction of the ice nucleation rate at T_N obtained in Equation S16 with the measured average ice nucleation delay τ_{av} at T_N (Note that Equation S16 predicts the nucleation rate at T_N). We obtain the needed λ-value by fitting the ice nucleation rate Equation S9 to the ice nucleation delay experiment shown in Fig. 3b and S1a. For $\alpha = -0.31$ K/min, Equation S16 yields $J(T_N) = 0.008\ \mathrm{s}^{-1}$ ($\tau_{av} = 1/J(T_N) = 125$ s). The so-predicted average ice nucleation delay agrees well with the measured τ_{av} in constant temperature experiments at T_N.

4. Geometrical factor *f*

The geometrical factor *f* of Equation S2 for the convex nanoroughness (bumps) is[1, 2]

$$f_v(m,R)=\frac{1}{2}\left\{1+\left(\frac{1-mx}{g_v}\right)^3+x^3\left[2-3\left(\frac{x-m}{g_v}\right)+\left(\frac{x-m}{g_v}\right)^3\right]+3mx^2\left(\frac{x-m}{g_v}-1\right)\right\} \quad , \qquad \text{(S22)}$$

where $g_v = (1-2mx+x^2)^{1/2}$, $x = R/r_c$ and $m=\cos(\Theta_{IW})$.

Similarly, the geometrical factor *f* for concave nanoroughness (pits) is[1]

$$f_c(m,R)=\frac{1}{2}\left\{1-\left(\frac{1+mx}{g_c}\right)^3-x^3\left[2-3\left(\frac{x+m}{g_c}\right)+\left(\frac{x+m}{g_c}\right)^3\right]+3mx^2\left(\frac{x+m}{g_c}-1\right)\right\} \quad , \qquad \text{(S23)}$$

where $g_c = (1+2mx+x^2)^{1/2}$, $x = R/r_c$ and $m=\cos(\Theta_{IW})$[1].

Fig. 2c and 2d show plots of the function *f* for both the convex and concave cases as a function of the ratio of roughness radius of curvature to the critical nucleus radius, *x*.

5. Surface Characterization

Fig. S2 shows the morphology of some investigated surfaces in addition to those shown in Fig. 1. The morphologies shown in Fig. S2 are the microstructure with larger pillar spacing and diameter (A2) and nanostructures with relatively larger roughness curvature radii (N2 - N5).

Fig. S3 depicts the advancing and receding contact angles measured on the surfaces tested in this work. The respective nanoscale roughness of the nanostructured surfaces and the geometrical parameters of the hierarchical surfaces are given in Table 1, 2 and 3, respectively. For a hydrophobic nanostructured surface, in general, increasing the roughness increases the advancing contact angle and the contact angle hysteresis (i.e. the difference between advancing and receding CAs). The inconsistencies in the trend (surfaces N2 and N4) can be interpreted as owing their origin to small, uncontrolled variation in nanoscale pitch of the surfaces, which is understandable given the dimensionally extreme nanostructuring employed.

For interpreting the advancing CAs on the hierarchical surfaces, we must evaluate the solid fraction of the surfaces. Since the advancing CA values in Fig. S3b are in the superhydrophobic range and receding CAs are not exceptionally high, we assume that the droplets are supported at the top of pillars (i.e. they are in the Cassie state) and denote the ratio of solid area under the droplet in actual contact with the liquid to the total apparent contact area enclosed by the contact line as Φ.[11] The lower the Φ, the higher the CA. With the inclusion of nanoroughness, the value of Φ will be reduced further; however, if we keep the nanoroughness the same, the Φ for the microstructure alone can be used to understand the trend in CA on the hierarchical surfaces. This is the reason why in Fig. S3b we see that the advancing CA for the A2/B2/C2-N2 surfaces (lower Φ) is higher than for the A1/B1/C1-N2 surfaces, irrespective of the actual pillar diameter and pitch.

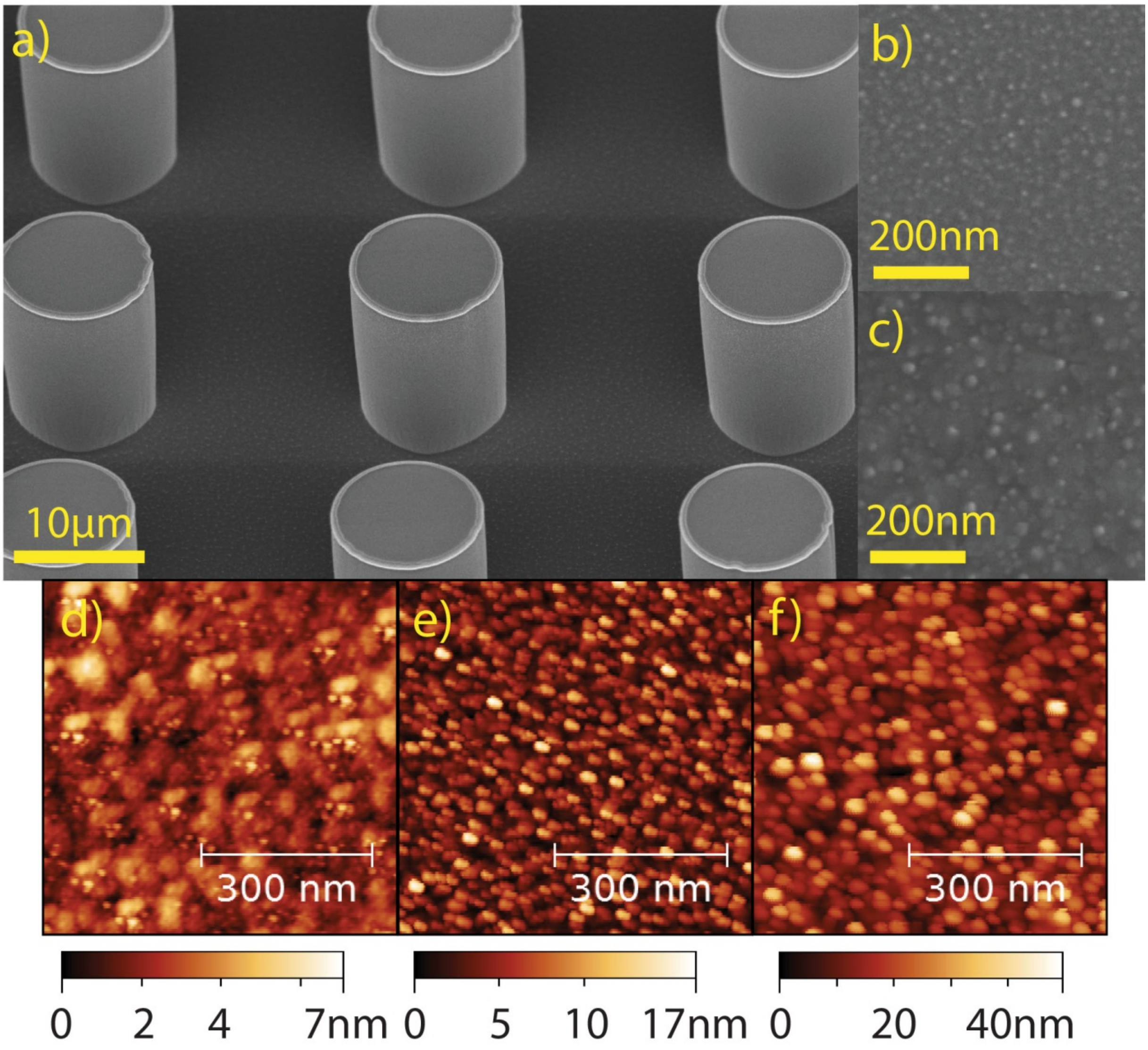

Fig. S2 Surface characterization. a) SEM image of A2 micropillar structure after ICP etching. A thin SiO_2 hardmask layer is on the top surface of the pillars. b-c) SEM image of nanostructure types N4 and N5, respectively. d-f) AFM scan of nanostructure types N3, N4 and N5, respectively.

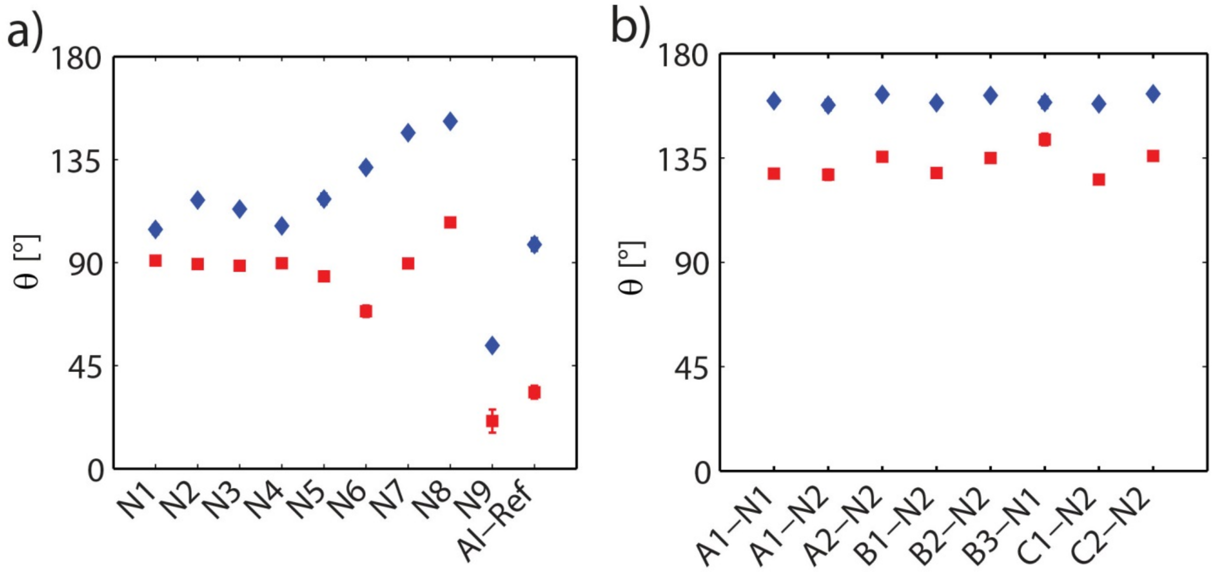

Fig. S3 Contact angle characterization. Water-air advancing (blue diamond) and receding (red squares) contact angles. a) Contact angles of nanostructured SiO_2 substrates and the reference aluminum substrate. Substrates N10 and N11 were completely wetting and are, thus, not shown. b) Contact angles of hydrophobic hierarchical micro-pillar substrates with SiO_2 nanostructure N2 and N1 coated with FDTS.

6. Nanoscale Interface Confinement Effect

Ice nucleation on any substrate is considerably influenced by the value of the contact angle between a forming, water-surrounded ice embryo, Θ_{IW}, and the substrate. In order to analyze nanoscale effects, which influence the heterogeneous nucleation on our substrates, we attempt to obtain the needed Θ_{IW} values. The Θ_{IW} of the classical heterogeneous nucleation theory can be regarded as temperature dependent and Θ_{IW} can be determined by solving for Θ_{IW} from Equation S1 and S2 at a specific temperature (for e.g. at T_N) by using the corresponding nucleation rate $J(T)$. To obtain Θ_{IW} from Equation S1 and S2, $\gamma_{IW}(T)$, $\Delta H_{f,v}(T)$ and $K(T)$ are set to the bulk values for the specific temperature. For the smooth hydrophobic substrate N1 and the smooth hydrophilic substrate N9, the nucleation rates are $J(T_N) = 1/125\ \mathrm{s} = 0.008\ \mathrm{s}^{-1}$ and $J(T_N) = 0.017\ \mathrm{s}^{-1}$ according Equation S16 and the results are $\Theta_{IW} = 99°$ at $T_N = -24.2$ °C and Θ_{IW} = 100° at $T_N = -24.4$ °C, respectively. In solving for $\Theta_{IW},$ the fact was utilized that the roughness curvature radii R of N1 and N9 remain well above $10r_c$ ($R/r_c >> 1$) hence, the roughness radius of curvature R does not affect the factor f of Equation S2.

Given the same material composition for our hydrophobic substrates (N1 through N8), an analysis of the ice nucleus and the substrate interface is needed to examine how Θ_{IW} depends on surface curvature for nanostructured surfaces. This fact is directly relevant to the important finding of insensitivity of median nucleation temperature with roughness on our nanoscale surfaces and is discussed in the following.

The ice nucleation on nanostructured surfaces must account for the existence of a quasiliquid layer between the ice nucleus and the solid substrate. Unequivocal experimental and computational results have substantiated the existence of a disordered amorphous layer at the surface of ice clusters[12], which have similar size as ice nuclei, and the disordering can reach a liquid like state at the interface ice with vapors and solids.[13, 14] Measurements pertaining to the presence of quasiliquid layer on ice in contact with SiO_2[14] and hydrophobic alkylsilanes treated substrates[15] clearly suggest that this must be factored in our analysis. The presence and thickness of such a quasiliquid, will naturally alter the free energy barrier for the formation of an ice nucleus and influence the heterogeneous nucleation process. Fig. 2e shows a schematic with the different interfaces present, due to the introduction of an interfacial quasiliquid layer between a curved solid substrate and a nascent ice nucleus. As we will show, the presence of such a quasiliquid layer at the interface between a nanoscale cavity and the nascent ice nucleus has profound influence on freezing of supercooled liquid on nanostructured surfaces. We refer to this phenomenon, which leads to a change in ice-water contact angle in a nano-cavity and thus fundamentally alters the nucleation characteristics, as nanoscale interface confinement effect.

A simple balance of the interfacial forces(see Fig. 2e) yields a modified Young's Equation

$$\cos(\theta_{IW})\frac{\gamma_{IW}}{\beta}=\gamma_{SW}-\gamma_{SLL}-\frac{\gamma_{ILL}}{\beta}=\left(\gamma_{SW}+\frac{\gamma_{IW}}{\beta}-\gamma_{SI}\right)\mathrm{e}^{\frac{-d}{\xi}}-\frac{\gamma_{IW}}{\beta},$$

(S24)

where γ_{ILL}, γ_{SLL}, γ_{SI} and γ_{SW} denote the surface energies of the interface between ice and quasiliquid layer, substrate and quasiliquid layer, substrate and ice, and substrate and liquid, respectively. $\beta=\left(\frac{R}{R-d}\right)^2$ and the symbols d and ξ represent the thickness of the quasiliquid layer and the decay length of the interaction with the bulk.[16] In Equation S24 the relations $\gamma_{ILL}=\gamma_{IW}\left(1-\mathrm{e}^{\frac{-d}{\xi}}\right)$ and $\gamma_{SLL}=\gamma_{SI}\,\mathrm{e}^{\frac{-d}{\xi}}+\gamma_{SW}\left(1-\mathrm{e}^{\frac{-d}{\xi}}\right)$ were used.[16]

Equation S24 can be rewritten as

$$\cos(\theta_{IW})=\left[\cos(\theta_{IW})^{*}\beta+1\right]e^{\frac{-(d-d^{*})}{\xi}}+(1-\beta)e^{\frac{-d}{\xi}}-1, \tag{S25}$$

where Θ_{IW}^{*}, d^{*} denote the ice-water contact angle and the thickness of the quasiliquid layer on a flat substrate ($R=\infty$).

From Equation S25, for $R >> d$ one obtains

$$\cos(\theta_{IW})\approx\left(\cos(\theta_{IW})^{*}+1\right)e^{\frac{-(d-d^{*})}{\xi}}-1. \tag{S26}$$

Equations S25 and S26 predict the increase in Θ_{IW} with an increase in the thickness of the quasiliquid layer. Equation S26 can be thought of as a mathematical representation of the nanoscale interface confinement effect.

The thickness of the quasiliquid layer can be determined by minimizing the excess of free energy of the water molecules at the ice-substrate interface. For example, if we consider a concave pit as a section of a sphere (see Fig. S2e), we can express the change in free energy associated with formation of the interface between the ice nucleus and the pit surface, i.e. the formation of the quasiliquid layer, as[16]

$$\Delta G = \frac{\Omega}{3}\left(R^3 - (R-d)^3\right)\Delta G_{f,v} + \Omega(R-d)^2\gamma_{IW} + \Omega R^2\left(\gamma_{SW} + \Delta\gamma e^{\frac{-d}{\xi}}\right) \tag{S27}$$

where Ω is the solid angle of the spherical section of the interface between the ice nucleus and the pit surface, and $\Delta\gamma = \gamma_{SI'} - \gamma_{SW} - \gamma_{IW}$. Interfaces exhibiting a quasiliquid layer require $\Delta\gamma > 0$. Thus, we obtain that $\gamma_{SI'} > \gamma_{SW} + \gamma_{IW}$. The quasiliquid layer thickness resulting from minimizing Equation S27 increases with decreasing pit radius and this in turn increases θ_{IW} according Equation S26. Setting $\partial\Delta G / \partial d = 0$ and $\partial^2\Delta G / \partial d^2 = 0$, from Equation S27, the linearized Gibbs-Thomson relation for melting point depression can be readily derived as

$$\Delta T \approx -T_m \frac{2\gamma_{IW}}{(R-d_m)H_{f,v}} \tag{S28}$$

where ΔT, d_m denote the depression of the melting point compared to the bulk melting point and the resulting thickness of the quasiliquid layer, respectively. For our substrates, Equation S27, yields $d_m \approx 0.6nm$ at T_m.

Fig. 2b compares the median nucleation temperature (T_N) curves for a surface with 15% of its area occupied by nanoscale pits. The curves were obtained by classical nucleation theory[1] for a constant Θ_{IW} = 100° (blue dashed line) and for a progressively increasing Θ_{IW} accounting for the presence of quasiliquid layer, i.e. the nanoscale interface confinement effect (black solid line). The latter clearly explains the relative insensitivity of T_N to nanotexture over three orders of magnitude of roughness RMS, as discussed in the main paper in the context of Fig. 2. Therefore, for surfaces with varying pit radii ice nucleation should predominantly take place at sites considered as flat in the sense of the classical nucleation theory ($R > 10r_c$). On the other hand, at constant Θ_{IW}, the T_N steadily increases for decreasing roughness radius of curvature until nearly the melting point depression curve (dotted red line, see Equation S28) is reached. Thereafter, for further decreasing pit radii[17], the freezing point curve follows the melting point depression curve.

Note that the above-described approach can also be exploited to analyze nucleation in the limit of a hypothetical surface comprised of an array of nanoscale pits shown by Fig. S4, i.e. where the pit coverage is 100%. The resulting T_N curve shown as black dash dotted line in Fig. 2*B*, upon accounting for the presence of the quasiliquid layer, steadily decreases for decreasing pit radius (i.e. increasing confinement), an effect generally observed in freezing experiments with nanoscale structures.[18] This provides a good validation for the above outline approach for the change in the T_N on nanotextured surfaces.

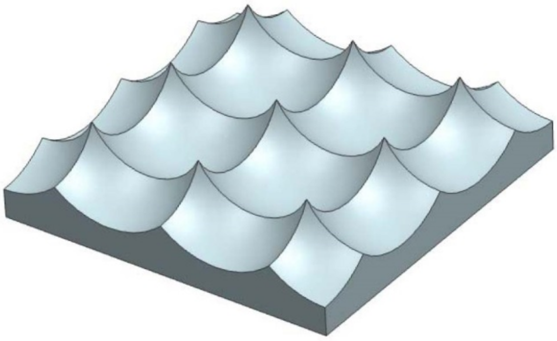

Fig. S4 Nanoscale pit surface. Hypothetical surface completely occupied with nanoscale pits.

7. Error Assessment

In our experiments for determining the nucleation temperature, the temperature was reduced at the slow rate of $\alpha = -0.31$ K/min to avoid any thermal gradients in the measurement chamber (see Fig. S6). The temperature decrease rate α fluctuated between +/−0.06 K/min around the average value of −0.31 K/min which results by employing Equation S14 in the uncertainty of the median nucleation temperature (T_N) to be +/−0.1 °C. For the ice nucleation delay measurements the error bars were obtained using statistical uncertainty analysis for the measured τ_{av} from Poisson statistics for a confidence level of 95%.[7]

8. Droplet Impact Experiment

Fig. S5 shows sequential snapshots of droplet impacts at Weber number (We) $\approx$ 30 and substrate temperature $T = -25$ °C for superhydrophobic substrate C1-N2 (a – f) and hydrophilic nanostructured surface N9 (g – l), respectively. The We is defined as $\rho V^2 D_w / \gamma_{wg}$, where V, D_w respectively denote the velocity and diameter of the impacting droplet, and ρ and γ_{wg} the density and surface tension of water. Clearly, the impacting droplet on the superhydrophobic substrate C1-N2 completely rebounds and the surface is free of water after the impact. In contrast, on the hydrophilic surface N9 the droplet adheres and wets the surface after the impact. We note that we conducted these experiments with room temperature droplets for practical reasons, as the water droplet would already freeze at the output of the dispenser unit at $T = -25$ °C. Despite this experimental simplification, we can show the higher droplet impact resistance of the superhydrophobic surface compared to the hydrophilic substrate at subcooled substrate temperature conditions. For an icephobic surface, it is desirable that it possesses a high liquid repellency and impact resistance.[10] In addition to the lower ice adhesion argument above, this explains why we pursued hierarchical hydrophobic surfaces with thermodynamically guided tailoring of their nanostructured morphology, leading to extraordinary ice nucleation delay.

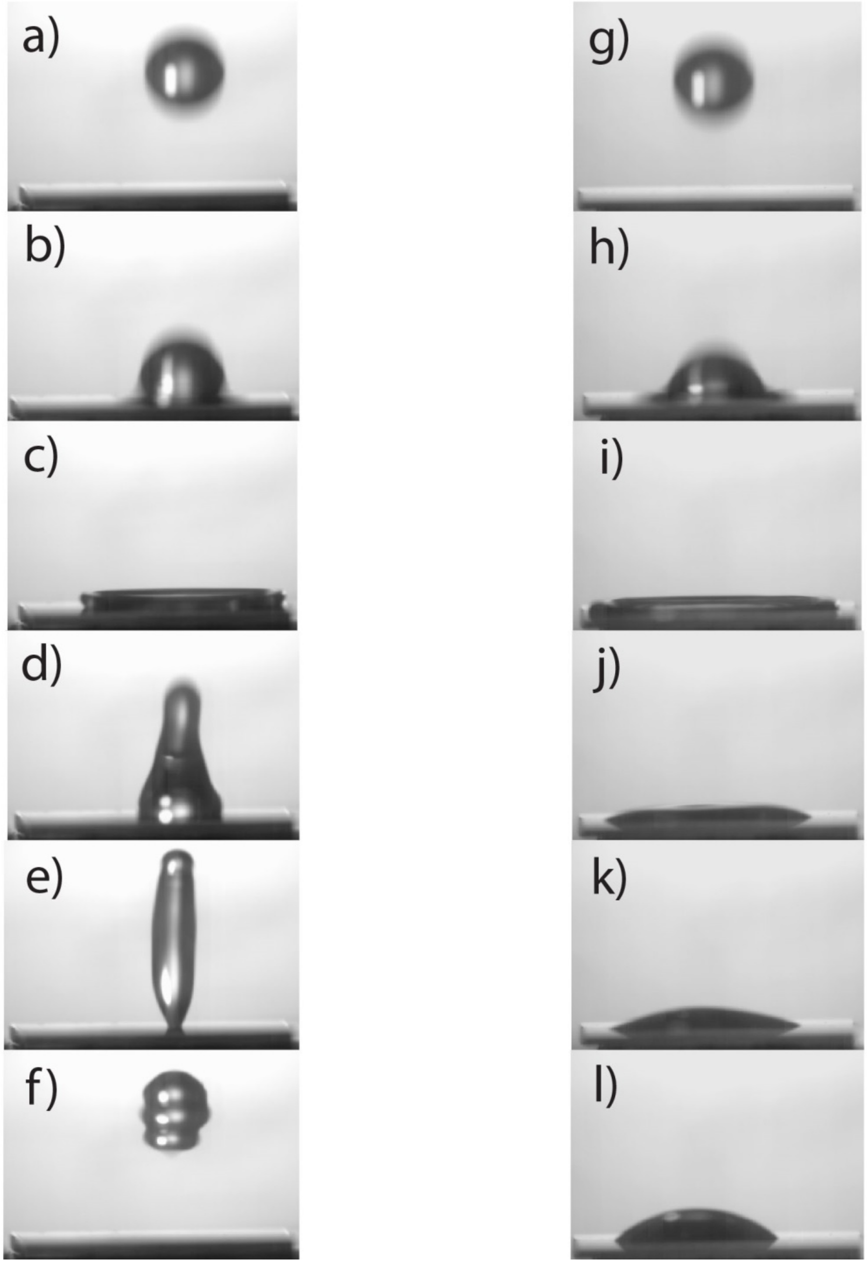

Fig. S5 Droplet impact experiment. Sequential snapshots of droplet impact experiments at We ≈ 30 and substrate temperature $= -25$ °C. a-f) impact on superhydrophobic substrate showing complete droplet rebound and a water-free surface after impact. g-l) impact on hydrophilic nanostructured surface N9. Droplet adheres to and remains on the surface.

9. Experimental Methods

Surface preparation. *Microfabrication:* A 500 nm thick layer of SiO_2 was deposited by plasma enhanced chemical vapor deposition (PECVD) on clean p-doped Si wafers to serve as hard mask for ICP etching. SiO_2 coated wafers were patterned with pillar geometries by photolithography. Shipley S1813 photoresist was used for photolithography. The lithographically developed pattern was transferred into SiO_2 layer by reactive ion etching (RIE) with a CHF_3/Ar plasma, following which the photoresist was stripped with a solvent. Chips 8x8 mm in size were diced from the wafer and then etched in a cryogenic ICP machine (Oxford Instruments ICP 180) at −100 °C in SF_6/O_2. The height of the resulting micropillars was adjusted by altering the etching time. The hard-mask was removed in a 1:5 diluted 40% HF solution.

Nanostructuring: The nanostructure N2 was obtained by PECVD of a 60 nm SiO_2 layer in an Oxford Instruments PECVD 80+ machine. For N3, first a 60 nm of SiO_2 layer was deposited by PECVD and then 1 nm layer of gold was added upon it using electron beam induced (e-beam) evaporation in a Plassys evaporator forming gold dots of 10-15 nm diameter. The low surface interaction energy between gold and SiO_2 leads to the formation of dots instead of a uniform gold film.[19] The Au-dots were subsequently passivated by a second PECVD deposition of a 2 nm SiO_2 layer. N4 consists of a 60 nm SiO_2 layer, which subsequently was etched using cryogenic ICP for 2 minutes. N5 and N6 were initially coated with 400 nm SiO_2 and N7, N10, N11 with 2.4μm SiO_2. Substrates N5, N6, N7, N10 and N11 were then etched with ICP for 4, 9, 72, 36 and 72 minutes, respectively. Nanostructure N8 was fabricated by glancing angle deposition (angle of deposition 85°) of 400 nm thick titanium using e-beam evaporation resulting in the formation of nanopillars. To generate hierarchical morphologies, the required nanostructuring was applied after the micropillars were formed.

To generate hydrophobic samples, the surface energy was lowered with a self assembled monolayer coating of 1H,1H,2H,2H-Perfluorodecyltrichlorosilane (FDTS) $C_{10}H_4Cl_3F_{17}Si$ (96 % Alfa Aesar). Before the monolayer application, the substrates were activated in a high frequency low pressure oxygen plasma for 10 minutes. After activation, the surface was hydrolyzed by placing the substrates into a water vapor saturated vessel for 10 minutes, at room temperature. Immediately afterwards, the substrates were immersed for one minute in a 1.3 mM solution of FDTS in ultra-pure n-hexane solution. Only traces of water are required in the n-hexane solution for the reaction to form a uniform monolayer, so that we did not additionally increase the water content in the solution. After the wet chemical treatment in the FDTS solution, the substrates were washed in ultra-pure n-hexane and then in ultra-pure isopropylalcohol (IPA). Finally, they were dried in a stream of nitrogen gas.

Surface characterization. AFM scans were performed in tapping mode using a super sharp silicon tip (tip radius 2 nm) in an Asylum Research AFM. The contact angle measurements were performed using an in house built goniometer-type system comprising of a syringe pump and a camera with a macro lens. Contact angles were determined with an imaging processing software (Photoshop®).

Droplet impact was recorded using a Phantom 9.1 high speed camera at 1000 frames per second (fps).

Experimental set-up. The experimental freezing setup, as illustrated in Fig. S6, was composed of an outer double layer chamber made of thermally insulating and optically transparent poly(methyl methacrylate) (PMMA). The transparency facilitated imaging of the sessile droplets undergoing freezing. The intervening space between the two layers in the chamber was evacuated to improve the insulation. A brass pipe fitted into the chamber was connected to a controlled, cold stream of nitrogen vapor in order to cool the chamber. The cold nitrogen stream was supplied by a cryogenic cooler, (Isotherm KGW TG-LKW-H) with a temperature control system. The small inner chamber ensured uniform environmental conditions around the droplet. The bottom surface of the chamber accommodated a table to support the substrates on which sessile droplets were place in order to record the ice nucleation temperatures. In order to control the humidity in the immediate environment of the droplets, an ice bath surrounded the table supporting the substrates. As a result, a spatially uniform and stable humidity condition could be maintained near the droplets under test. With this procedure, the humidity level was always saturated with respect to ice and corresponded to a relative humidity level of 80 % at −20 °C and to 75 % at −25 °C with respect to liquid water.[1] High humidity conditions suppress the possibility of homogeneous nucleation appearing due to evaporative cooling of the droplets.[20] A small sample access window at the top of the outer and inner chamber allowed the exchange of the substrate and the placement of droplets by a pipette. Before starting any test, both chambers were purged with nitrogen vapor and then all the open ports were closed. Two thermal sensors (Pt-1000 2I 161, IST AG) and a humidity sensor (LinPicco A0545, IST AG), marked respectively as T1, T2 and H1 in Fig. S6, were placed in the chamber to monitor the chamber conditions throughout the experiment. While T1 measured the table temperature, which was taken to be equal to the substrate temperature due to the high thermal conductivity of the substrate and the table material (brass), T2 sensed the ambient temperature of the inner chamber and H1 recorded the relative humidity. In addition, a high-speed camera with macro lens (resolution ~0.05 mm), not shown in Fig. S6, recorded the onset of freezing and allowed the observation of the nucleation process of the droplet.

Experimental protocols. We used two kinds of tests: nucleation temperature determination and ice nucleation delay measurement. In each case, freezing of the supercooled water droplet occurred in two distinct steps.[21] First a rapid recalescent stage (lasting ~ 10 ms) led to partial solidification of the droplet and turned it into a liquid solid mixture. This stage could be easily detected using our high speed video recording at 1000 frames per second, thus yielding a time resolution of 1 ms. The Movie S3 shows the first stage freezing on surface N1. The onset of freezing is marked by a clear change in droplet image intensity and thus easily detectable. Following the recalescent step, the drops froze completely through a second, slower and isothermal stage lasting ~ 10's of seconds. Movies S4 and S5 show this step on the surface N1 and A2-N2, respectively.

For the nucleation temperature measurements, initially the experimental chamber and the substrate were all maintained at −14 °C. Droplets with a volume of 4 μL were drawn out of a pot of melting ice of high purity water (Type 1 Ultrapure Milli-Q, resistivity > 18MΩcm), using a pipette, so their initial temperature was near 0 °C, and placed on the substrate. The temperature was kept at −14 °C until the condensation rim from the droplet placement had evaporated. Condensation occurs due to the temperature difference between droplet and substrate. The ambient near the sessile droplet was saturated with respect to ice-vapor equilibrium as described above. After initial equilibration, the temperature was then steadily lowered at a rate of −0.31 K/min until nucleation initiated. The error associated with changes in the cooling rate is minimal as discussed in Supplementary Information, section 7. The onset of nucleation was monitored by visual inspection and continuous recording, using a high-speed camera. The temperatures of the chamber and the substrate, and the chamber humidity were continuously monitored and recorded. For nucleation delay measurements the table and the substrate were first maintained at the constant experimental temperature, following which a droplet from melting ice pot was placed on the substrate. The delay time was measured from droplet placement until nucleation initiation.

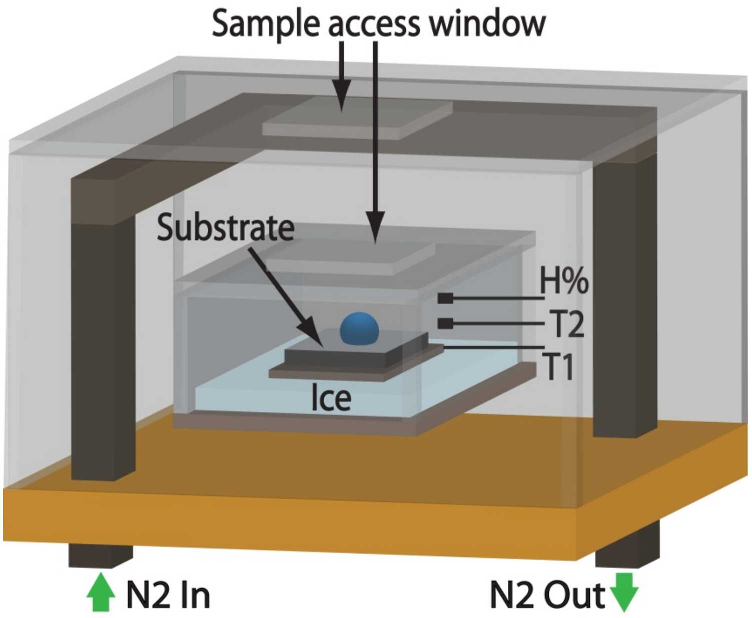

Fig. S6 Schematic of the freezing chamber comprised of an outer and an inner chamber. The inner chamber accommodated the tested substrates with a sessile droplet. An ice bath in the inner chamber kept the ambient around the droplet saturated with respect to ice during each freezing test.

Move S1. Droplet impact on a hierarchical superhydrophobic surface (C1-N2) at We ≈ 30 and substrate temperature $T = -25$ °C. The droplet completely rebounds (see also Supplementary Information, section 8). The high-speed recordings (at 1000 fps) have been slowed down 200 times in the videos.

Movie S2. Droplet impact on a hydrophilic nanostructured surface (N9) at We ≈ 30 and substrate temperature $T = -25$ °C. The droplet adheres to the hydrophilic substrate, see also Supplementary Information, section 8. The high-speed recordings (at 1000 fps) have been slowed down 200 times in the videos.

Movie S3. The initial, recalescent, quasi-adiabatic partial solidification of droplet on hydrophobic substrate N1 at -24 °C. This initial freezing front grows rapidly and randomly into the droplet and partially freezes the droplet in ~10 ms leaving a mixed ice-liquid phase in the droplet. The released latent heat of fusion is larger than the dissipated heat, as a consequence the droplet temperature rises to ~0 °C. The high-speed recordings (at 1000 fps) has been slowed down 500 times in the in Movie S3.

Movie S4. The slower isothermal freezing phase following the initial freezing phase on hydrophobic substrate N1 at -24 °C. This phase is dominated by the capability of the droplet-substrate interface to dissipate the released heat from the droplet solidification process. The ice-liquid mixture resulting from the initial recalescent stage of freezing solidifies starting from the substrate towards to the top of the droplet.

Movie S5. The slower isothermal freezing phase following the initial freezing phase on hydrophobic substrate A2-N2 at -25.5 °C. This phase is dominated by the capability of the droplet-substrate interface to dissipate the released heat from the droplet solidification process. The ice-liquid mixture resulting from the initial recalescent stage of freezing solidifies starting from the substrate towards to the top of the droplet.

References

[1] H. R. Pruppacher, J. D. Klett, *Microphysics of Clouds and Precipitation*, Vol. 18, Kluwer Academic Publishers, New York, Boston, Dordrecht, London, Moscow 1997.

[2] N. H. Fletcher, *J Chem Phys* **1958**, *29*, 572.

[3] B. Zobrist, T. Koop, B. P. Luo, C. Marcolli, T. Peter, *J Phys Chem C* **2007**, *111*, 2149.

[4] P. W. Atkins, *Physical Chemistry*, Oxford University Press, Oxford 1990.

[5] R. S. Smith, B. D. Kay, *Nature* **1999**, *398*, 788.

[6] F. Pellerey, M. Shaked, J. Zinn, *Probab Eng Inform Sc* **2000**, *14*, 353.

[7] T. Koop, B. P. Luo, U. M. Biermann, P. J. Crutzen, T. Peter, *J Phys Chem A* **1997**, *101*, 1117; R. Barlow, *Statistics : a Guide to the use of Statistical Methods in the Physical Sciences*, Wiley, Chichester, England ; New York 1989.

[8] M. J. Pellerite, E. J. Wood, V. W. Jones, *J Phys Chem B* **2002**, *106*, 4746.

[9] A. J. Meuler, J. D. Smith, K. K. Varanasi, J. M. Mabry, G. H. McKiney, R. E. Cohen, *ACS Appl Mater Inter* **2010**, *2*, 3100.

[10] L. Mishchenko, B. Hatton, V. Bahadur, J. A. Taylor, T. Krupenkin, J. Aizenberg, *ACS Nano* **2010**, *4*, 7699.

[11] A. Lafuma, D. Quere, *Nat Mater* **2003**, *2*, 457.

[12] C. C. Pradzynski, R. M. Forck, T. Zeuch, P. Slavicek, U. Buck, *Science* **2012**, *337*, 1529; V. Buch, S. Bauerecker, J. P. Devlin, U. Buck, J. K. Kazimirski, *Int Rev Phys Chem* **2004**, *23*, 375.

[13] G. Malenkov, *J Phys-Condens Mat* **2009**, *21.*

[14] S. Engemann, H. Reichert, H. Dosch, J. Bilgram, V. Honkimaki, A. Snigirev, *Phys Rev Lett* **2004**, *92.*

[15] M. Mezger, S. Schoder, H. Reichert, H. Schroder, J. Okasinski, V. Honkimaki, J. Ralston, J. Bilgram, R. Roth, H. Dosch, *J Chem Phys* **2008**, *128.*

[16] R. R. Vanfleet, J. M. Mochel, *Surf Sci* **1995**, *341*, 40.

[17] S. J. Cooper, C. E. Nicholson, J. Liu, *J Chem Phys* **2008**, *129*.

[18] G. H. Findenegg, S. Jahnert, D. Akcakayiran, A. Schreiber, *Chemphyschem* **2008**, *9*, 2651; J. Liu, C. E. Nicholson, S. J. Cooper, *Langmuir* **2007**, *23*, 7286.

[19] J. Albuschies, M. Baus, O. Winkler, B. Hadam, B. Spangenberg, H. Kurz, *Microelectron Eng* **2006**, *83*, 1530.

[20] S. Jung, M. K. Tiwari, N. V. Doan, D. Poulikakos, *Nat Commun* **2012**, *3*.

[21] S. Jung, M. Dorrestijn, D. Raps, A. Das, C. M. Megaridis, D. Poulikakos, *Langmuir* **2011**, *27*, 3059.